



Article

Enhanced Catalytic Reduction of 4-Nitrophenol Driven by Fe₃O₄-Au Magnetic Nanocomposite Interface Engineering: From Facile Preparation to Recyclable Application

Yue Chen ^{1,2,†}, Yuanyuan Zhang ^{1,2}, Qiangwei Kou ^{1,2}, Yang Liu ^{1,2,*}, Donglai Han ^{3,†}, Dandan Wang ⁴, Yantao Sun ^{1,2}, Yongjun Zhang ^{1,2}, Yaxin Wang ^{1,2}, Ziyang Lu ⁵, Lei Chen ^{1,2}, Jinghai Yang ^{1,2} and Scott Guozhong Xing ^{6,*}

¹ College of Physics, Jilin Normal University, Siping 136000, China; 17649973053@163.com (Y.C.); 13944139606@163.com (Y.Z.); 13944949603@163.com (Q.K.); syt@jlnu.edu.cn (Y.S.); yjzhang@jlnu.edu.cn (Y.Z.); wangyaxin1010@126.com (Y.W.); chenlei@jlnu.edu.cn (L.C.); jhyang1@jlnu.edu.cn (J.Y.)

² Key Laboratory of Functional Materials Physics and Chemistry of the Ministry of Education, Jilin Normal University, Changchun 130103, China

³ School of Materials Science and Engineering, Changchun University of Science and Technology, Changchun 130022, China; dlhan_1015@cust.edu.cn

⁴ Technology Development Department, GLOBALFOUNDRIES (Singapore) Pte. Ltd., 60 Woodlands Industrial Park D, Street 2, Singapore 738406, Singapore; DANDAN.WANG@globalfoundries.com

⁵ School of Environment and Safety Engineering, Jiangsu University, Zhenjiang 212013, China; lzy@mail.ujs.edu.cn

⁶ United Microelect Corp. Ltd., 3 Pasir Ris Dr 12, Singapore 519528, Singapore

* Correspondence: liuyang@jlnu.edu.cn (Y.L.); guozhongupenn@gmail.com or Scott_Xing@UMC.com (S.G.X.); Tel./Fax: +86-434-329-4566 (Y.L. & S.G.X.)

† These authors contributed equally to this work.

Received: 23 April 2018; Accepted: 18 May 2018; Published: 22 May 2018



Abstract: In this work, we report the enhanced catalytic reduction of 4-nitrophenol driven by Fe₃O₄-Au magnetic nanocomposite interface engineering. A facile solvothermal method is employed for Fe₃O₄ hollow microspheres and Fe₃O₄-Au magnetic nanocomposite synthesis via a seed deposition process. Complementary structural, chemical composition and valence state studies validate that the as-obtained samples are formed in a pure magnetite phase. A series of characterizations including conventional scanning/transmission electron microscopy (SEM/TEM), Mössbauer spectroscopy, magnetic testing and elemental mapping is conducted to unveil the structural and physical characteristics of the developed Fe₃O₄-Au magnetic nanocomposites. By adjusting the quantity of Au seeds coating on the polyethyleneimine-dithiocarbamates (PEI-DTC)-modified surfaces of Fe₃O₄ hollow microspheres, the correlation between the amount of Au seeds and the catalytic ability of Fe₃O₄-Au magnetic nanocomposites for 4-nitrophenol (4-NP) is investigated systematically. Importantly, bearing remarkable recyclable features, our developed Fe₃O₄-Au magnetic nanocomposites can be readily separated with a magnet. Such Fe₃O₄-Au magnetic nanocomposites shine the light on highly efficient catalysts for 4-NP reduction at the mass production level.

Keywords: Fe₃O₄ hollow microspheres; Fe₃O₄-Au magnetic nanocomposites; catalytic reduction; 4-nitrophenol

1. Introduction

Nowadays, numerous nitroaromatic compounds have been discharged into rivers with the overuse of dyes, explosives and pesticides in industry, causing serious water pollution [1]. Regrettably, 4-nitrophenol (4-NP) is the most typical toxic and refractory organic pollutant, attacking the eco-systems of both humans, as well as animals and consequently promoting various diseases [2]. Therefore, the degradation of 4-NP into non-toxic small molecules and in turn preventing harm has become a research hotspot in recent years [3,4].

Although it is difficult to degrade 4-NP due to the high stability and low solubility of 4-NP in water, many semiconductor nanomaterials (such as, ZnO [5], Cu₂O [6] and TiO₂ [7]) and various methods (e.g., typical photocatalysis and chemical catalysis [8]) have been developed to solve the pollution problems of 4-NP. Generally, the catalytic conversion of 4-NP to 4-aminophenol (4-AP) is an imperative process, using excess sodium borohydride as the reducing agent, not only because 4-AP is less toxic than 4-NP, but also because 4-AP is in demand on the market in many industrial fields [9]. Unfortunately, the reduction process of 4-NP to 4-AP is very slow by NaBH₄ alone. Therefore, the use of catalysts is necessary to enable electron transfer from donor B[−]H₄[−] to acceptor 4-NP [10].

Most recently, noble metal nanocrystals have received both fundamental and practical attention owing to their potential applications in many fields such as ultrasensitive biosensing [11], imaging agents [12], photothermal therapy [13], catalysts [14], etc. Especially, Au nanoparticles (NPs) have been intensely explored because of their unique and tunable optical properties and high catalytic activities [15–19]. Compared to the semiconductor photocatalysts, noble metal catalysts possess higher catalytic activity with respect to organic pollutants [20–24]. Typically, Au NPs have been intensely employed for the catalytic reduction of a variety of organic pollutants [25]. However, Au NPs tend to agglomerate to form clusters due to their high surface area, reducing their intrinsic high catalytic activities [26,27]. To restrain the aggregation of Au NPs, considerable research efforts have been devoted to immobilization of Au NPs onto various supporting materials [28]. Several excellent reviews discussed that the stability of Au NPs could be significantly improved through solid supporting materials, such as carbon, silica, magnetic materials, and so on [29–31]. Among the various above-mentioned supports, iron oxides have received much more attention because they can be readily separated with a magnet and thereby possess the advantage of being magnetically recoverable and recyclable [32–36].

Theoretically, the shape and the size of the Fe₃O₄ play a deterministic role in defining the chemical and physical properties of Fe₃O₄ owing to the shape anisotropy [37]. For instance, the nanomaterials with a hollow structure have potential application prospects as catalysis and in biotechnology due to their higher load efficiency compared to other solid structures [38]. Therefore, Fe₃O₄ hollow microspheres have become the focus of study owing to their large specific surface area, excellent magnetic properties and hollow structural characteristics, allowing multiple different molecules to be loaded [39]. Notably, it is hard to directly attach Au NPs to the surfaces of the Fe₃O₄ hollow microspheres owing to the dissimilar nature of the two species' surfaces. The use of the mediating “glue” layer of polymers supplying a certain kind of functional group is necessary, which not only can combine Au NPs with Fe₃O₄ hollow microspheres, but also enhance the stability, water solubility and the biocompatibility of nanomaterials [40]. For example, Wang et al. [41] reported that polyethyleneimine (PEI) could self-assemble on the surfaces of Fe₃O₄ to form a polymer shell, thus adhering to Au NPs via the abundant amine groups. However, the weak electrostatic interactions among positively-charged amino groups and negatively-charged Au NPs are unreliable, resulting in the partial separation of Au NPs from the polymers. Yan et al. [42] prepared bifunctional Fe₃O₄/Au nanocomposites by the direct reduction of HAuCl₄ in the presence of carboxylate-functionalized Fe₃O₄ particles. Liu and co-workers [43] recently discovered that the bidentate ligands with two chelating sulfur groups such as the dithiocarbamates (DTCs) featuring carbodithioate (CS₂) groups were more stable than other common ligands such as thiol and amino groups in adsorbing onto the surfaces of Au

NPs, indicating that the PEI-DTC polymers may boost the Au NPs' adhesive force onto Fe_3O_4 hollow microspheres' surfaces.

In this work, by adjusting the addition rounds of Au seeds, the amount of Au seeds coating the modified surfaces of Fe_3O_4 hollow microspheres can be well controlled, and the corresponding optical, magnetic and catalytic performances are investigated. Fe_3O_4 -Au magnetic nanocomposites consisting of Fe_3O_4 hollow microspheres, PEI-DTC polymers and Au NPs are successfully utilized as effective nanocatalysts for the reduction of 4-NP to 4-AP by NaBH_4 . The aim of this study is to provide a new generation of magnetic nanocomposites with high catalytic efficiency and recyclable application to organic pollutants. The preparation and catalytic process to 4-NP of the Fe_3O_4 -Au magnetic nanocomposites are shown in Figure 1.

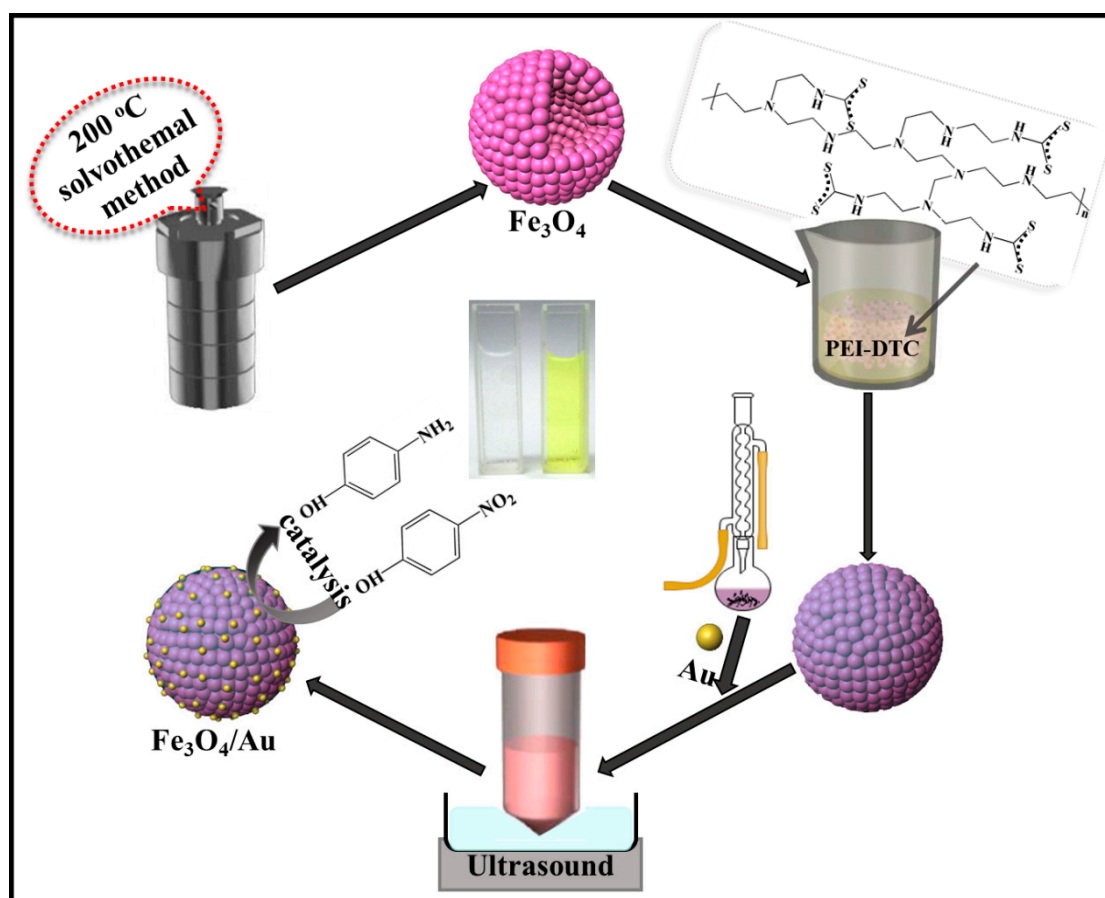


Figure 1. Schematic illustration of the fabrication process and catalytic application to 4-nitrophenol (4-NP) of Fe_3O_4 -Au magnetic nanocomposites. PEI-DTC, polyethyleneimine-dithiocarbamate.

2. Experimental Section

2.1. Materials' Development

Chemicals, including methanol, polyethyleneimine (PEI, branched, MW \approx 25,000 g/mol) and carbon disulfide (CS_2), were purchased from Aladdin industrial Co., Ltd. (Shanghai, China). Iron chloride hydrate ($\text{FeCl}_3 \cdot 6\text{H}_2\text{O}$) was purchased from Shanghai Macklin Biochemical Co., Ltd. (Shanghai, China). Ethylene glycol (EG), sodium dodecyl sulfate (SDS), sodium acetate ($\text{NaAc} \cdot 3\text{H}_2\text{O}$), potassium hydroxide (KOH), sodium citrate dihydrate ($\text{Na}_3\text{C}_6\text{H}_5\text{O}_7 \cdot 2\text{H}_2\text{O}$), 4-nitrophenol (4-NP) and gold (III) chloride hydrate ($\text{HAuCl}_4 \cdot 3\text{H}_2\text{O}$), were purchased from Sinopharm Chemical Reagent Co., Ltd. (Shanghai, China). The aforementioned reagents were analytical grade and were utilized without further purification.

2.2. Synthesis of Fe_3O_4 Hollow Microspheres

In a typical synthesis process for the Fe_3O_4 hollow microspheres, 1.62 g $\text{FeCl}_3 \cdot 6\text{H}_2\text{O}$ were dispersed in 60 mL EG into a beaker with mechanical stirring at room temperature. After 30 min, 2.70 g $\text{NaAc} \cdot 3\text{H}_2\text{O}$ and 0.1839 g SDS were added to the mixture. The mixture solution was vigorously stirred for 1 h until it became homogeneous. Then, the mixture was transferred to the Teflon-lined stainless steel autoclave, and it was kept at 200 °C for 12 h. After the samples were cooled to room temperature naturally, the products were obtained by centrifuging, sequentially rinsed with ethanol and deionized water for five times and subsequently dried under vacuum at 60 °C over night to obtain the Fe_3O_4 hollow microspheres.

2.3. Gold Seeds Synthesis

Approximately 80 mg $\text{Na}_3\text{C}_6\text{H}_5\text{O}_7 \cdot 2\text{H}_2\text{O}$ were dissolved in 8 mL deionized water. Two milliliters of 58 mM $\text{HAuCl}_4 \cdot 3\text{H}_2\text{O}$ were diluted into 198 mL of deionized water with vigorous stirring. The mixture was subsequently heated under reflux at 105 °C. The well-prepared sodium citrates were steadily added dropwise. The reaction mixtures were sustained for 15 min under stirring and reflux, leading to a buff to burgundy color change. The mixture was eventually cooled down to room temperature naturally.

2.4. PEI-DTC Synthesis

Five hundred milligrams of PEI (0.02 mmol) and 650 mg KOH (11.6 mmol) were dissolved in 50 mL methanol under magnetic stirring with completely dissolved KOH. The solution was then purged with N_2 for 15 s in order to exhaust the oxygen thoroughly, and 695 μL of CS_2 (11.6 mmol) was added by dripping slowly into the mixed solution. PEI-DTC was obtained with stirring for 10 min with a solution color change to light yellow.

2.5. Fe_3O_4 @PEI-DTC-Au Seeds' Synthesis

In this step, the surfaces of Fe_3O_4 hollow microspheres were functionalized with PEI-DTC. Ten milligrams of Fe_3O_4 hollow microspheres were washed with methanol three times. PEI-DTC solution droplets were injected with a pipette under vortexing. The developed mixture was then kept for 1 h. The precipitate was gathered with a dedicated external magnet and rinsed with deionized water three times to remove the unnecessary PEI-DTC. Finally, Fe_3O_4 @PEI-DTC NPs were re-dispersed in deionized water.

In comparison with counterpart bulk composites, equipped with a large surface area, the nanostructured materials demonstrate superior optical, magnetic and electrical characteristics [44–48]. The preparation of Fe_3O_4 @PEI-DTC-Au seed nanocomposites is as follows. The as-obtained 10 mL of gold seed colloids were added dropwise into the 4 mL of Fe_3O_4 @PEI-DTC NPs. Then, Fe_3O_4 @PEI-DTC-Au nanocomposites were rinsed with deionized water and the same process repeated, and the sample was named as Fe_3O_4 -Au 20 mL. Additional samples were prepared with the same conditions as Fe_3O_4 -Au 20 mL, while the amount of gold seed colloids was changed to 40 and 60 mL, named as Fe_3O_4 -Au 40 mL and Fe_3O_4 -Au 60 mL, respectively.

2.6. Application of Fe_3O_4 -Au Magnetic Nanocomposites for Catalytic Reduction of 4-NP

The catalytic ability of Fe_3O_4 -Au magnetic nanocomposites was performed in a cuvette with 1 mg of Fe_3O_4 -Au for the reduction of 4-NP (0.005 mol/L, 1 mL) in the presence of NaBH_4 (0.2 mol/L, 1 mL). The UV-Vis spectrophotometer was used to record the catalytic reduction rate at different time intervals in the scanning range of 200–500 nm.

In order to study the recyclability of the prepared Fe_3O_4 -Au magnetic nanocomposites, the samples were collected with a magnet from the reaction solution when the reduction process was completed. The obtained magnetic nanocomposites were rinsed with deionized water and ethanol

three times and then repeated in the next reaction. The same catalytic reduction process to 4-NP was repeated six times.

2.7. Characterizations

The structure and morphology of the samples were characterized by X-ray diffractometer (XRD) (Rigaku D/Max-2500, Rigaku Corporation, Tokyo, Japan), Mössbauer spectrum (FAST Comtec Mössbauer system, FAST Comtec, Oberhaching, Germany), X-ray photoelectron spectroscopy (XPS) (Thermo Scientific ESCALAB 250Xi, Thermo Fisher Scientific, Waltham, MA, USA), field-emission scanning electron microscopy (FESEM) (JEOL JSM-7800F, JEOL Ltd., Tokyo, Japan) and transmission electron microscope (TEM) (JEOL 2100, JEOL Ltd., Tokyo, Japan). Ultraviolet-visible spectroscopy (UV-Vis) spectra and magnetic properties were measured with a Shimadzu UV 3600 spectrophotometer (Shimadzu Corporation, Tokyo, Japan) and a quantum design MPMS3 superconducting quantum interference device (SQUID) magnetometer (Quantum Design, Inc., San Diego, CA, USA), respectively.

3. Results and Discussion

3.1. X-ray Diffraction of the Fe_3O_4 -Au Magnetic Nanocomposites

Figure 2a shows XRD patterns of the as-obtained pure Fe_3O_4 hollow microspheres and Fe_3O_4 -Au magnetic nanocomposites with the various amounts of gold seed colloids added (Fe_3O_4 -Au 5 mL, Fe_3O_4 -Au 20 mL, Fe_3O_4 -Au 40 mL and Fe_3O_4 -Au 60 mL). As for the pure Fe_3O_4 hollow microspheres, the diffraction peaks located at 30.4° , 35.5° , 43.4° , 53.4° , 57.3° and 62.8° were indexed to (220), (311), (400), (422), (511) and (440) of Fe_3O_4 (Joint Committee on Powder Diffraction Standards, JCPDS 19-0629), respectively [21,49]. The average crystallite size of the pure Fe_3O_4 hollow microspheres was about 576.5 nm calculated by the Debye–Scherrer equation [50]. Four additional peaks of Fe_3O_4 -Au magnetic nanocomposites at about 38.4° , 44.5° , 64.7° and 77.5° could be assigned into the (111), (200), (220) and (311) of Au (JCPDS 04-0784), respectively, suggesting the coexistence of Fe_3O_4 and Au [51,52]. Figure S1 presents the Pawley refinement of the XRD pattern of the pure Fe_3O_4 hollow microspheres. The residual weighted profile R-factor (Rwp) of the sample is 15.74%, which indicates that the sample is in agreement with the standard magnetite Fe_3O_4 . In addition, it is well established that the area of the diffraction peak of XRD patterns is proportional to the contents of that phase in the mixture. Increasing addition times of gold seed colloids enhanced the diffraction peaks of Au, implying that the number of the gold seeds coating the surfaces of Fe_3O_4 hollow microspheres increases.

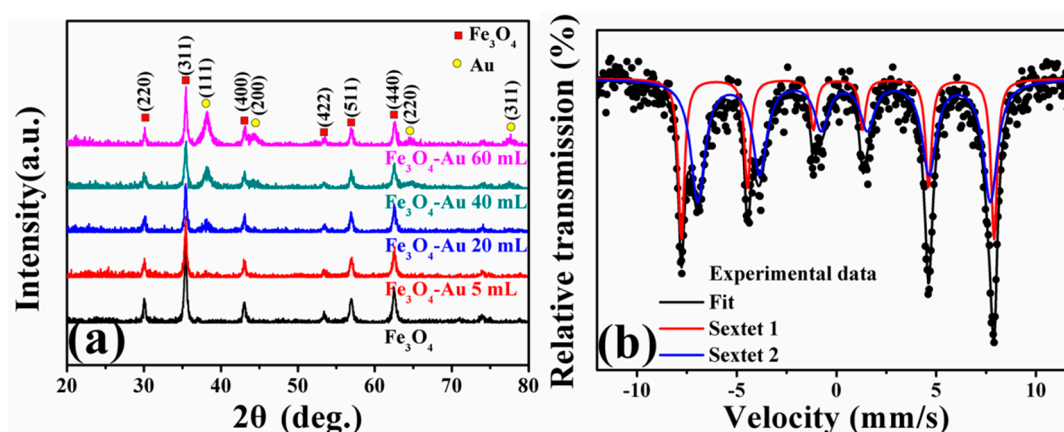


Figure 2. XRD patterns of the as-prepared pure Fe_3O_4 hollow microspheres and Fe_3O_4 -Au magnetic nanocomposites with the different addition quantities of the gold seed colloids (Fe_3O_4 -Au 5 mL, Fe_3O_4 -Au 20 mL, Fe_3O_4 -Au 40 mL and Fe_3O_4 -Au 60 mL) (a); Mössbauer spectra of pure Fe_3O_4 hollow microsphere (b).

Because magnetite Fe_3O_4 and maghemite $\gamma\text{-Fe}_2\text{O}_3$ have nearly the same crystal structure of an inverse spinel type, it is difficult to differentiate them only based on the XRD results. The Mössbauer spectrum is an available characterization technique to distinguish magnetite from maghemite [53,54]. Mössbauer spectra of Fe_3O_4 hollow microspheres fitted with two sextets (Zeeman splitting patterns) are shown in Figure 2b. The acute and strong lines of the magnetic sextets show a characteristic double six-peak structure of magnetite Fe_3O_4 [55]. The hyperfine field is 48.5 and 45.5 Tesla, and the isomer shift is 0.603 and 0.287 mm/s, corresponding to Fe^{2+} and Fe^{3+} ions at octahedral interstitial sites and Fe^{3+} ions at tetrahedral interstitial sites, respectively. Table 1 lists the fitted Mössbauer parameters. All these results testify that the as-obtained sample is a pure magnetite Fe_3O_4 instead of maghemite $\gamma\text{-Fe}_2\text{O}_3$ and consistent with the results reported by Ghosh et al. [56]. In fact, the oxidation product of the magnetite Fe_3O_4 is either maghemite $\gamma\text{-Fe}_2\text{O}_3$ or hematite $\alpha\text{-Fe}_2\text{O}_3$, which strongly depends on the oxidation temperature. Generally, a high temperature heat treatment is necessary to realize the phase transition of magnetite Fe_3O_4 , which indirectly suggests that the structure of magnetite Fe_3O_4 is stable at room temperature [57,58].

Table 1. Mössbauer spectrum parameters of pure Fe_3O_4 hollow microspheres: IS is the isomer shift, QS the quadrupole splitting, HIN the hyperfine field, HWHM the half width at half maximum and AREA the relative absorption area.

Composition	IS (mm/s)	QS (mm/s)	HIN (T)	HWHM (mm/s)	AREA (%)
A	0.287	0.015	48.5	0.186	34.3
B	0.603	0.012	45.5	0.433	65.7

3.2. Morphology of the Fe_3O_4 -Au Magnetic Nanocomposites

The specific structure and morphology of the developed Fe_3O_4 -Au magnetic nanocomposites were studied by TEM and SEM. In particular, TEM measurement is an effective methodology for structure research in materials science and materials engineering [59–71]. Figure 3 displays SEM and TEM images of pure Fe_3O_4 hollow microspheres. It can be observed that the pure Fe_3O_4 hollow microspheres are spherical shape. The average crystallite size is about 576 nm, and the samples show the narrow size distribution, as shown in Figure S2. TEM and SEM images of Fe_3O_4 -Au 5 mL, Fe_3O_4 -Au 20 mL, Fe_3O_4 -Au 40 mL and Fe_3O_4 -Au 60 mL are presented in Figure 4 and Figure S3. The as-prepared Fe_3O_4 -Au magnetic nanocomposites consist of the Fe_3O_4 hollow microspheres and the gold seeds of about 16 nm in diameter. Clearly, the gold seeds are randomly and homogeneously attached to the surfaces of the Fe_3O_4 hollow microspheres. Gold seeds are seen black, and Fe_3O_4 hollow microspheres present a light color in the TEM images, attributed to the higher electron density of Au compared to that of Fe_3O_4 [72]. It can be easily observed from the high-resolution TEM (HRTEM) image in the inset of Figure 4b that the interplanar distance values are 0.204 and 0.217 nm, matching the (220) lattice plane of Fe_3O_4 and the (111) lattice plane of Au, respectively [73]. The selected area electron diffraction (SAED) pattern of Fe_3O_4 -Au 40 mL is presented in the inset of Figure 4c, consisting of both the (220), (311), (400) and (511) diffraction rings of Fe_3O_4 and the (111), (200), (220) and (311) diffraction rings of Au [43]. The HRTEM and SAED results further verify the coexistence of Fe_3O_4 and Au. An interesting finding is that when increasing Au seed colloids' addition times, the gold seed contents on Fe_3O_4 surfaces are further boosted, which is consistent with the aforementioned XRD data. This is supported by the following elemental mapping images.

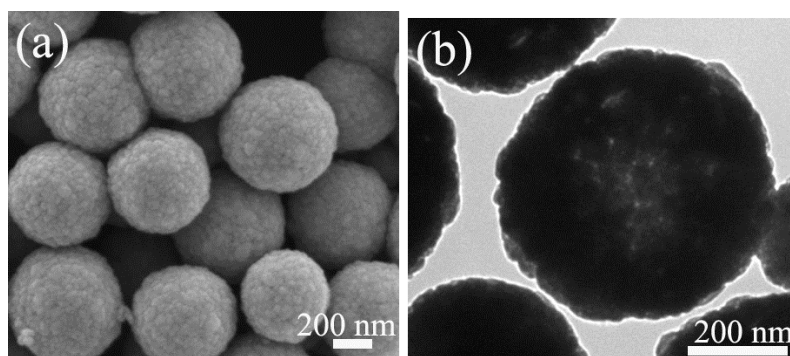


Figure 3. SEM images (a) and TEM images (b) of pure Fe_3O_4 hollow microspheres.

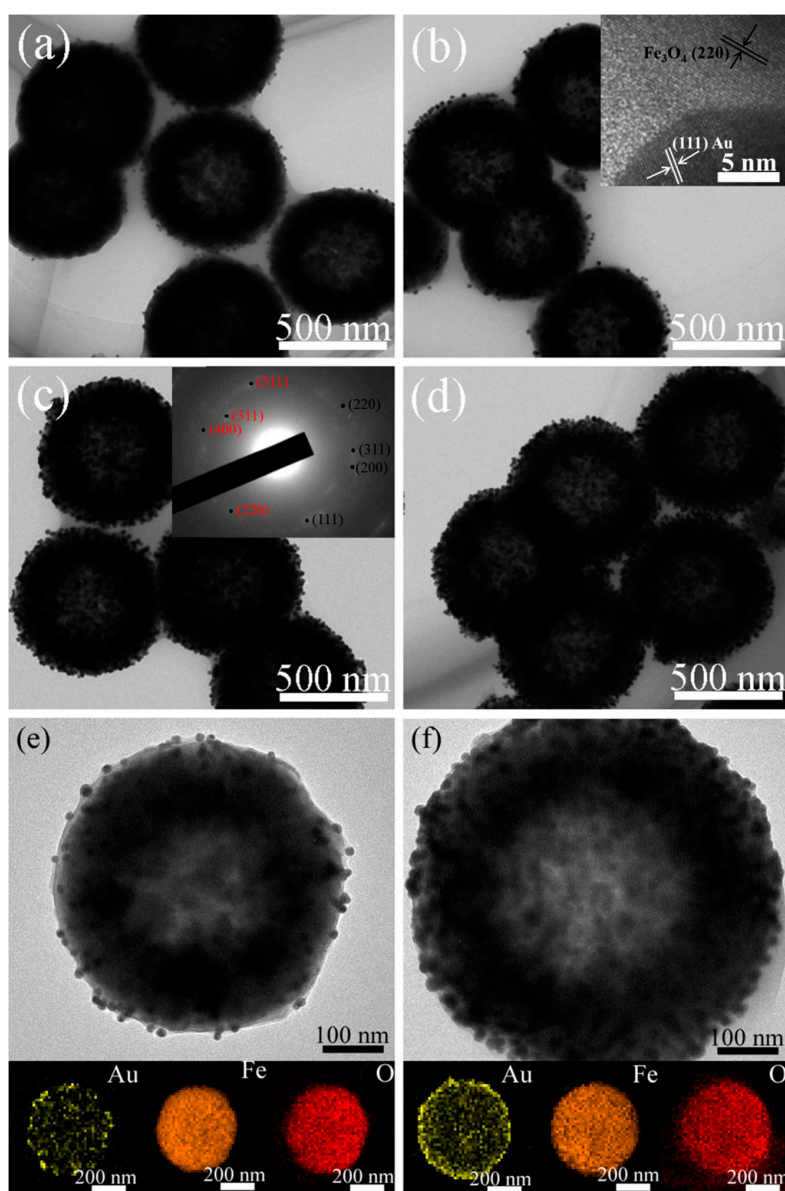


Figure 4. TEM images of Fe_3O_4 -Au 5 mL (a) and Fe_3O_4 -Au 20 mL with the HRTEM image (inset) (b), Fe_3O_4 -Au 40 mL with the SAED pattern (inset) (c) and Fe_3O_4 -Au 60 mL (d). TEM images of single Fe_3O_4 -Au 5 mL (e) and Fe_3O_4 -Au 60 mL (f) microspheres and corresponding EDS elemental mapping images (Au, Fe and O).

Figure 4e,f shows the TEM images of single Fe_3O_4 -Au 5 mL and Fe_3O_4 -Au 60 mL microspheres and corresponding energy-dispersive X-ray (EDS) mapping images of Au, Fe and O elements [74,75]. It could be clearly found that the Fe_3O_4 hollow microspheres have hollow internal structures, and Au seeds are homogeneously attached to the surfaces of the Fe_3O_4 hollow microspheres. In addition, compared with Fe_3O_4 -Au 5 mL, the amount of gold seeds on the surfaces of Fe_3O_4 for Fe_3O_4 -Au 60 mL increases significantly.

3.3. Optical Properties of the Fe_3O_4 -Au Magnetic Nanocomposites

UV-Vis spectroscopy studies are carried out to investigate the optical properties of pure Fe_3O_4 hollow microspheres and Fe_3O_4 -Au magnetic nanocomposites. Figure 5 presents the UV-Vis spectra of pure Fe_3O_4 hollow microspheres, Au seed colloids, Fe_3O_4 -Au 5 mL, Fe_3O_4 -Au 20 mL, Fe_3O_4 -Au 40 mL and Fe_3O_4 -Au 60 mL magnetic nanocomposites. No absorption peak is observed for the pure Fe_3O_4 hollow microspheres in the visible wavelength span [34,76]. The Au gold seed colloids display a characteristic surface plasmon resonance (SPR) peak at ~ 520 nm on account of the coherent excitation of the free electrons within the conduction band [77]. In addition, all the Fe_3O_4 -Au magnetic nanocomposites show a clear characteristic SPR band of gold nanostructures. Interestingly, the absorption peak of Fe_3O_4 -Au magnetic nanocomposites is broadened and shows a slight red shift compared with that of pure Au seed colloids. The more Au seeds are deposited on Fe_3O_4 hollow microspheres' surfaces, the more evident the red shift of the absorption peak is. The absorption band shows a red-shift from 526 nm for Fe_3O_4 -Au 5 mL to 540 nm for Fe_3O_4 -Au 60 mL. This red shift of the SPR absorption band can be ascribed to plasmon hybridization and the surface plasmon coupling of neighboring Au seeds deposited on Fe_3O_4 hollow microspheres [52,78].

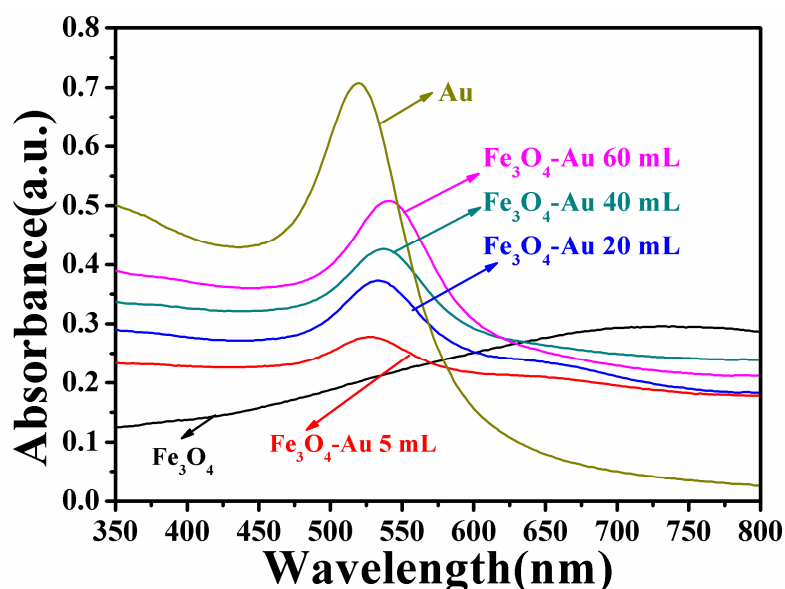


Figure 5. UV-Vis absorption spectra of pure Fe_3O_4 hollow microspheres, Au seed colloids, Fe_3O_4 -Au 5 mL, Fe_3O_4 -Au 20 mL, Fe_3O_4 -Au 40 mL and Fe_3O_4 -Au 60 mL magnetic nanocomposites.

3.4. XPS of the Fe_3O_4 -Au Magnetic Nanocomposites

XPS was applied to characterize the elemental chemical states and chemical compositions of the pure Fe_3O_4 hollow microspheres and Fe_3O_4 -Au magnetic nanocomposites. The C 1s peak at 284.8 eV is applied as the reference for charge correction [79]. The XPS results of Fe_3O_4 , Fe_3O_4 -Au 5 mL, Fe_3O_4 -Au 20 mL, Fe_3O_4 -Au 40 mL and Fe_3O_4 -Au 60 mL are shown in Figure 6. Figure 6a is the high-resolution scans of the XPS spectra for Fe 2p. The binding energy of pure Fe_3O_4 hollow microspheres is assessed at 711.2 and 724.5 eV by using Gaussian-Lorentzian fitting and assigned to

the Fe 2p_{3/2} and Fe 2p_{1/2} of magnetite Fe₃O₄, respectively [80]. As for Fe₃O₄-Au 20 mL (Figure 6b), the peak doublet appearing at 83.9 and 87.9 eV with a spin orbit splitting of ~4 eV is assigned to Au 4f_{7/2} and Au 4f_{5/2}, respectively [81]. It is important to highlight that with the increase of the quantity of the Au seeds on the Fe₃O₄ surfaces, the intensity of Fe 2p decreases and the intensity of Au 4f increases, because the intensity of XPS spectra is proportional to the atomic concentration and the atomic sensitivity factor [82]. Meanwhile, Fe 2p-associated peaks shift toward lower binding energy, while Au 4f peaks shift toward the opposite binding energy side. The shift in binding energy provides evidence of an interaction between Au and Fe₃O₄. The chemical shifts in the Fe 2p peaks and Au 4f peaks are probably caused by the transfer of charge carriers at the metal-oxide interfaces [83–85]. As shown in Figure 6c, the O 1s spectrum of pure Fe₃O₄ exhibits only a single peak at 532.8 eV, and no obvious shift of peak position is observed [86]. The survey scan results demonstrate that all the indexed peaks correspond to those of Fe, Au, O and C (Figure 6d).

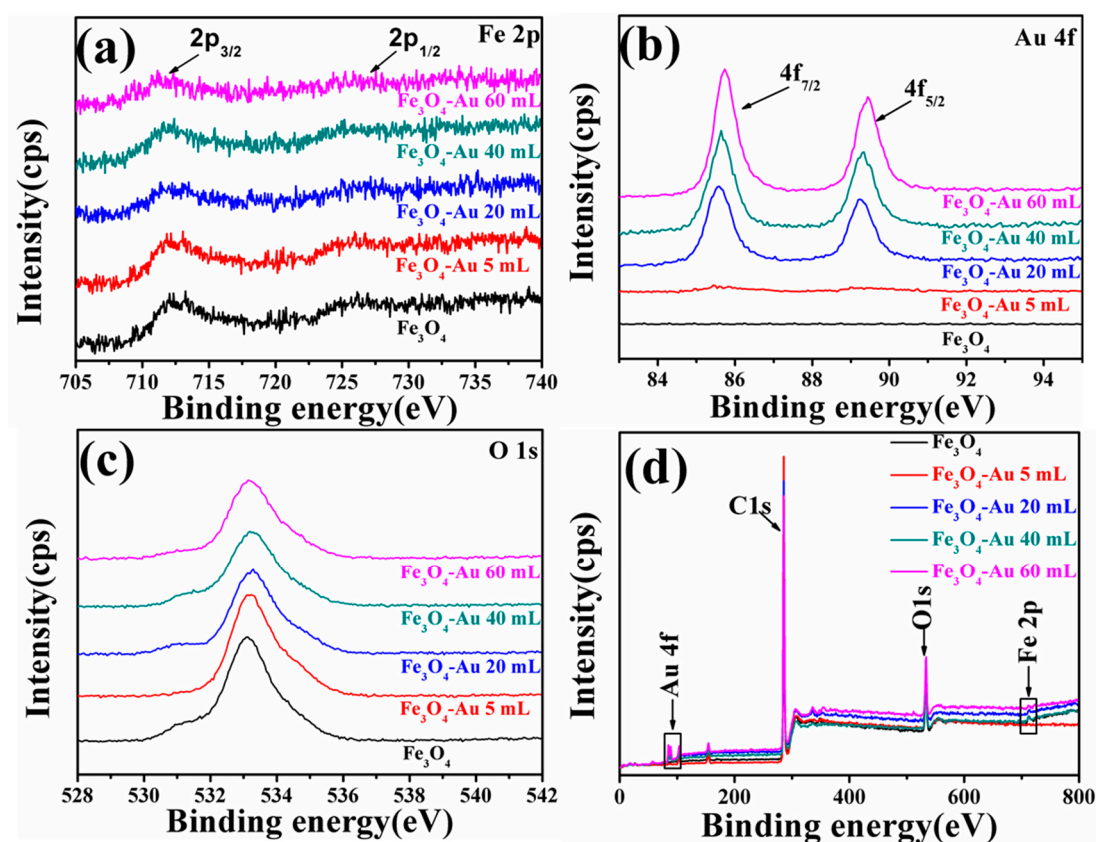


Figure 6. XPS spectra of the as-obtained Fe₃O₄, Fe₃O₄-Au 5 mL, Fe₃O₄-Au 20 mL, Fe₃O₄-Au 40 mL and Fe₃O₄-Au 60 mL: the Fe 2p binding energies (a), the Au 4f binding energies (b), the O1s binding energies (c) and XPS survey spectra (d).

3.5. Magnetic Properties of the Fe₃O₄-Au Magnetic Nanocomposites

The magnetic properties of the obtained samples were measured using SQUID. The magnetization versus magnetic field (M-H) loops of pure Fe₃O₄ hollow microspheres and Fe₃O₄-Au magnetic nanocomposites are presented in Figure 7. The M-H loops of all the samples are S-shaped curves and exhibit negligible coercivity and remanence, which is the typical characteristic of superparamagnetic nanomaterials [87]. Moreover, in order to confirm the superparamagnetism of the as-obtained sample, the temperature-dependent magnetization (M-T) on pure Fe₃O₄ hollow microspheres was measured under zero-field-cooled (ZFC) and 1000 Oe field-cooled (FC) conditions (Figure S4). With the increase of temperature, the magnetization increases to a maximum at the blocking temperature and then

decreases, consistent with the superparamagnetic behavior [88]. The saturation magnetization (M_s) of pure Fe_3O_4 hollow microspheres reaches up to 93.2 emu/g, but the M_s value of Fe_3O_4 -Au 5 mL reduces to 88.1 emu/g. Further coating with the gold seeds results in a continuous decrease of the M_s value. As for Fe_3O_4 -Au 60 mL, the M_s value is only 68.6 emu/g. The gradual decrease in the M_s value can be ascribed to the increase in the weight ratio of Au seeds to Fe_3O_4 hollow microspheres or the diamagnetic contribution of the Au seeds deposited onto the surfaces of the Fe_3O_4 hollow microspheres [89–91]. It must also be mentioned that although M_s values decrease owing to the introduction of Au seeds, the Fe_3O_4 -Au magnetic nanocomposites retain the strong magnetic responsivity and can be easily magnetically collected from aqueous solution by the magnet (as shown in the inset of Figure 7), which is beneficial to their economic and reusable applications.

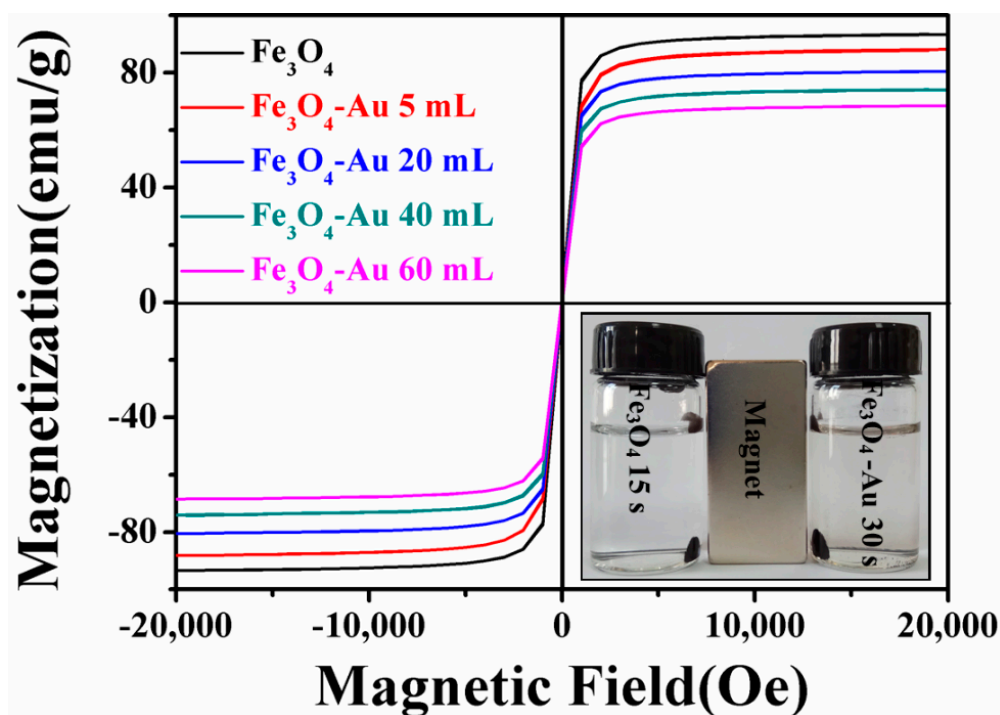


Figure 7. Magnetic hysteresis (M-H) loops of Fe_3O_4 , Fe_3O_4 -Au 5 mL, Fe_3O_4 -Au 20 mL, Fe_3O_4 -Au 40 mL and Fe_3O_4 -Au 60 mL. The inset is the photograph of pure Fe_3O_4 hollow microspheres and Fe_3O_4 -Au 60 mL magnetic nanocomposites in deionized water after using a magnet.

3.6. Catalytic Activity of Fe_3O_4 -Au Magnetic Nanocomposites to 4-NP

To study the catalytic performance of Fe_3O_4 -Au magnetic nanocomposites to organic pollutants, the catalytic reduction of 4-NP in the presence of excess NaBH_4 was selected as a model reaction. As shown in Figure S5, the original aqueous 4-NP solution has a maximum absorption peak at 317 nm. If the catalysts are absent, the absorption peak at 317 nm is unchanged even after a couple of days [20]. Once freshly obtained NaBH_4 solution is added, the absorption peak at 317 nm shifts to 400 nm due to the formation of 4-nitrophenolate ions, and meanwhile, the color of the mixture changes from light yellow to dark yellow [92]. However, the reduction reaction cannot be produced without gold seeds even in the presence of excess NaBH_4 , as can be testified in Figure S6. There is almost no change in the intensity at 400 nm after 480 min, indicating that the addition of pure Fe_3O_4 hollow microspheres has little influence on the reduction of 4-NP. Figure 8 exhibits UV-Vis absorption spectra of 4-NP catalyzed by the different Fe_3O_4 -Au magnetic nanocomposites (Fe_3O_4 -Au 5 mL, Fe_3O_4 -Au 20 mL, Fe_3O_4 -Au 40 mL and Fe_3O_4 -Au 60 mL) in the presence of NaBH_4 at a certain time interval. When Fe_3O_4 -Au magnetic nanocomposites are introduced into the reaction system, the absorption peak of all the samples at 400 nm decreases in intensity. At the same time, a new peak located at 300 nm

appears and increases concomitantly in intensity with the reaction time, which is attributed to the formation of 4-AP, the corresponding product in the reduction of 4-NP. The whole peak at 400 nm disappears after 40, 12, 4 and 2 min catalyzed by $\text{Fe}_3\text{O}_4\text{-Au}$ 5 mL, $\text{Fe}_3\text{O}_4\text{-Au}$ 20 mL, $\text{Fe}_3\text{O}_4\text{-Au}$ 40 mL and $\text{Fe}_3\text{O}_4\text{-Au}$ 60 mL, respectively. The color of the solution transforms from yellow to colorless, demonstrating that the 4-NP is completely changed into 4-AP and no other byproducts are generated. The corresponding pseudo-first-order plots of $\ln(C/C_0)$ versus reaction time over different $\text{Fe}_3\text{O}_4\text{-Au}$ magnetic nanocomposites are portrayed in Figure 9. The concentration of NaBH_4 is identified as a constant because it is much more excessive compared to that of 4-NP. The ratio of C (the concentration of 4-NP at reaction time t) to C_0 (the initial concentration of 4-NP) is obtained from the relative intensity of respective absorbance (A_t/A_0) at 400 nm. The linear relationship of $\ln(C/C_0)$ against reaction time represents that the reduction of 4-NP by the $\text{Fe}_3\text{O}_4\text{-Au}$ magnetic nanocomposites follows the pseudo first order kinetics. The rate constant (k) can be calculated by a liner plot of $\ln(C/C_0)$ vs. reduction time. The rate constants of 4-NP are 0.0738, 0.228, 0.857 and 3.031/min using $\text{Fe}_3\text{O}_4\text{-Au}$ 5 mL, $\text{Fe}_3\text{O}_4\text{-Au}$ 20 mL, $\text{Fe}_3\text{O}_4\text{-Au}$ 40 mL and $\text{Fe}_3\text{O}_4\text{-Au}$ 60 mL as nanocatalysts, respectively. Obviously, the rate constants for 4-NP reduction increase when increasing Au seed addition rounds. It is reasonable that if the noble metal nanomaterials' loading is increased, the mass fraction of the noble metal nanomaterials is higher in the final samples, and thus, a better catalytic performance should be accomplished [93]. We thus propose that the catalytic capability of $\text{Fe}_3\text{O}_4\text{-Au}$ magnetic nanocomposites could be greatly improved when more gold seeds cover the surfaces of the Fe_3O_4 hollow microspheres.

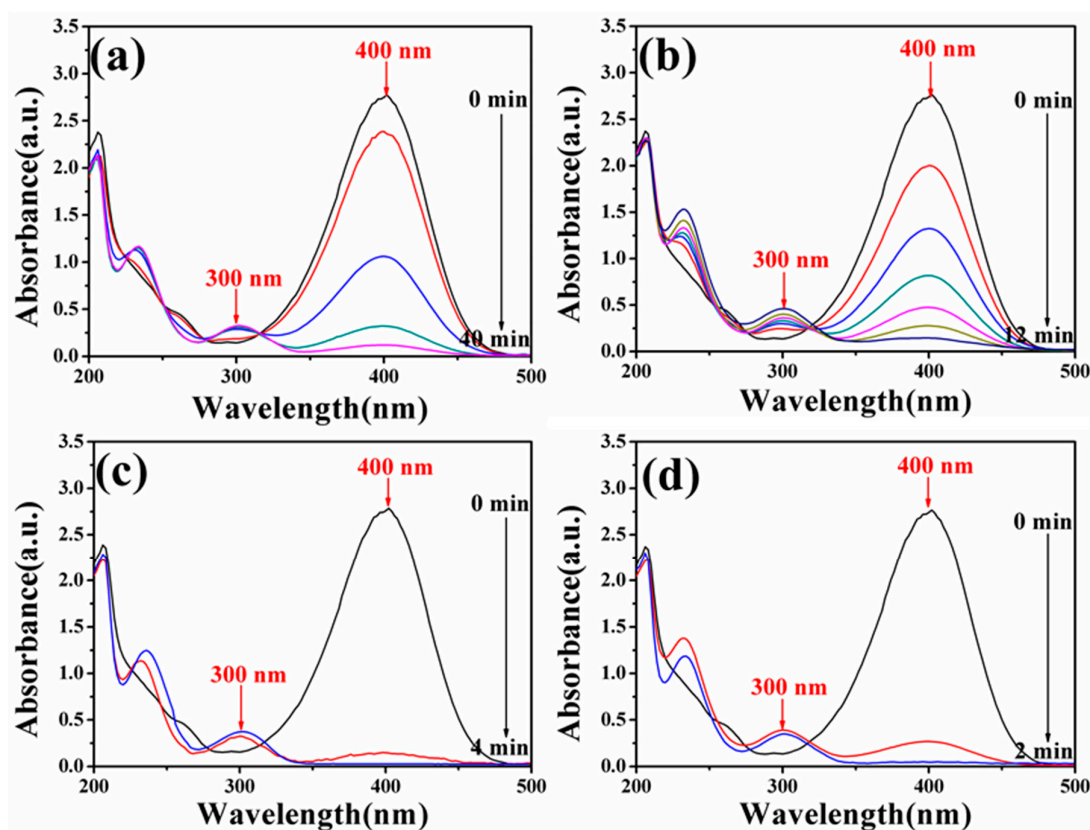


Figure 8. UV-Vis absorption spectra of 4-NP after reduction catalyzed by $\text{Fe}_3\text{O}_4\text{-Au}$ 5 mL (a), $\text{Fe}_3\text{O}_4\text{-Au}$ 20 mL (b), $\text{Fe}_3\text{O}_4\text{-Au}$ 40 mL (c) and $\text{Fe}_3\text{O}_4\text{-Au}$ 60 mL (d).

To implement the practical application of $\text{Fe}_3\text{O}_4\text{-Au}$ magnetic nanocomposites, their stability and the recyclability are essential. All the $\text{Fe}_3\text{O}_4\text{-Au}$ magnetic nanocomposites were separated magnetically and reused after catalytic reduction of 4-NP. As shown in Figure 10, all the samples can be successfully reused for at least six reaction runs for the catalytic reduction of 4-NP, elaborating that the $\text{Fe}_3\text{O}_4\text{-Au}$

magnetic nanocomposites possess the excellent stability and can serve as recoverable and efficient nanocatalysts of the organic pollutants.

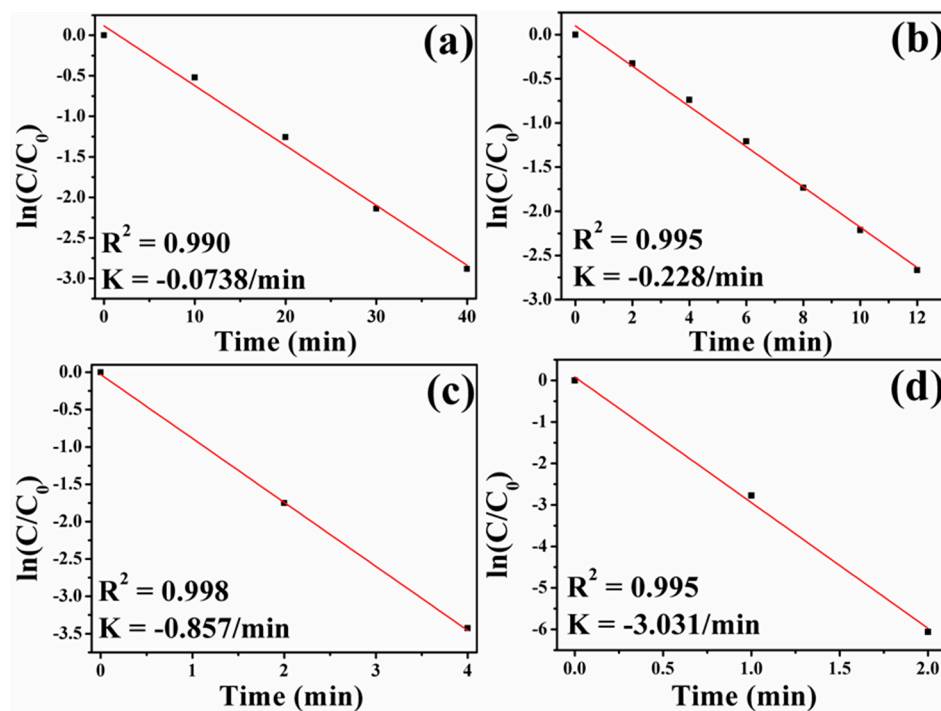


Figure 9. Plots of $\ln(C/C_0)$ against reaction time: $\text{Fe}_3\text{O}_4\text{-Au}$ 5 mL (a), $\text{Fe}_3\text{O}_4\text{-Au}$ 20 mL (b), $\text{Fe}_3\text{O}_4\text{-Au}$ 40 mL (c) and $\text{Fe}_3\text{O}_4\text{-Au}$ 60 mL (d).

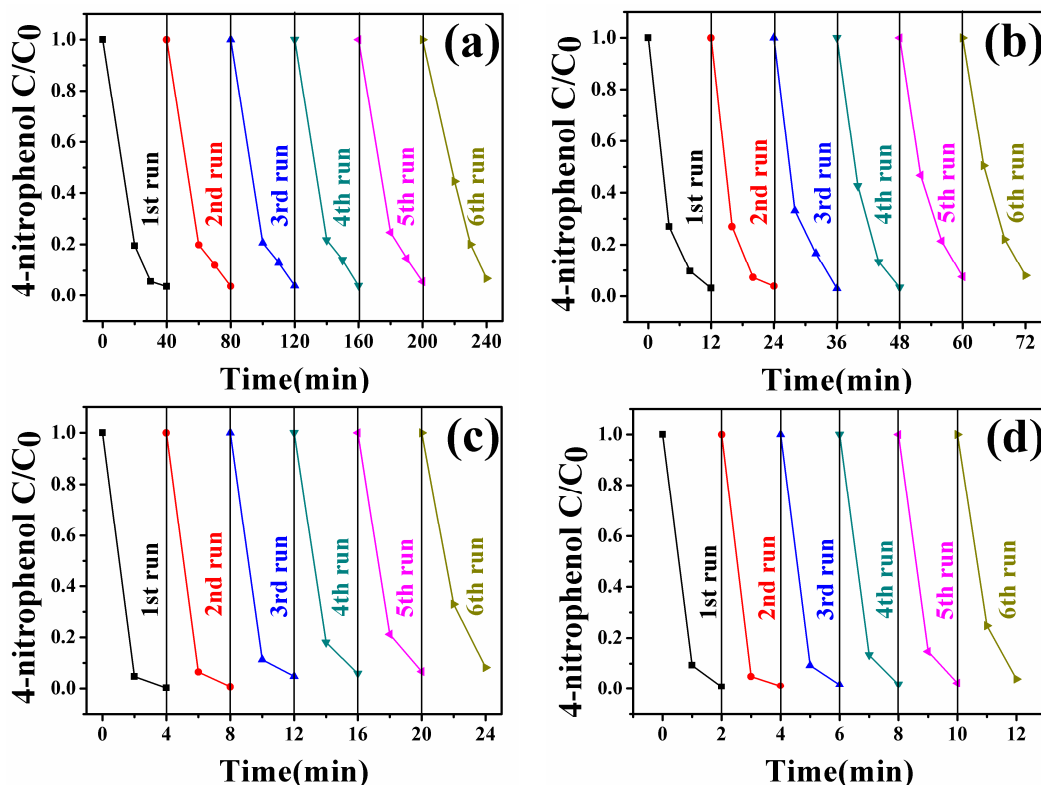


Figure 10. Reusability of $\text{Fe}_3\text{O}_4\text{-Au}$ 5 mL (a), $\text{Fe}_3\text{O}_4\text{-Au}$ 20 mL (b), $\text{Fe}_3\text{O}_4\text{-Au}$ 40 mL (c) and $\text{Fe}_3\text{O}_4\text{-Au}$ 60 mL (d) for catalytic reduction of 4-NP.

4. Conclusions

In summary, Fe₃O₄-Au magnetic nanocomposites were prepared by a well-developed seed deposition method. Structural analyses confirmed that the as-prepared Fe₃O₄-Au magnetic nanocomposites possessed a high surface area and that the gold seeds were homogeneously deposited onto the Fe₃O₄ hollow microspheres' surfaces. The increase of the quantity of the gold seeds attached to the surfaces of the Fe₃O₄ hollow microspheres results in Fe 2p peaks shifting toward a lower binding energy and Au 4f peaks shifting towards a higher binding energy. Although the Ms value decreases with the increase of the gold seed amount deposited on the Fe₃O₄ surfaces, the samples retain the strong magnetic responsivity and can be easily collected by a magnet. The pseudo-first-order kinetics are used to calculate the rate constant of 4-NP, and the rate constants for the 4-NP reduction increase when increasing the added amount of gold seeds. Furthermore, Fe₃O₄-Au magnetic nanocomposites can serve as recyclable nanocatalysts for 4-NP. Therefore, Fe₃O₄-Au magnetic nanocomposites can be excellent nanocatalysts for the catalytic reduction of organic pollutants in the treatment of waste water.

Supplementary Materials: The following are available online at <http://www.mdpi.com/2079-4991/8/5/353/s1>. Figure S1: Pawley refinement of the XRD pattern of the pure Fe₃O₄ hollow microspheres. Red dots, blue lines and olive bars represent the experimental data, the calculated data and the peak position of the sample, respectively. The bottom line in black shows the different experimental-calculated data, Figure S2: Particle size distribution obtained from the analysis of the TEM images for pure Fe₃O₄ hollow microspheres, Figure S3: SEM and corresponding EDS images of the as-prepared Fe₃O₄-Au nanocomposites with the different addition quantities of the gold seed colloids (Fe₃O₄ (a, b and c), Fe₃O₄-Au 5 mL (d, e and f), Fe₃O₄-Au 20 mL (g, h and i), Fe₃O₄-Au 40 mL (j, k and l) and Fe₃O₄-Au 60 mL (m, n and o), Figure S4: ZFC and FC curves of pure Fe₃O₄ hollow microspheres under an applied field of 1000 Oe, Figure S5: UV-Vis absorption spectra of 4-NP before (red line) and after adding NaBH₄ solution (black line), Figure S6: UV-Vis absorption spectra of 4-NP catalyzed by pure Fe₃O₄ hollow microspheres in presence of NaBH₄ before and after 480 min.

Author Contributions: Conceptualization, Y.L. and S.G.X.; Software, D.W.; Validation, Z.L. and L.C.; Formal Analysis, Y.Z.; Data Curation, Q.K.; Writing-Original Draft Preparation, Y.C. and D.H.; Writing-Review & Editing, Y.S., Y.Z. and Y.W.; Supervision, J.Y.; Funding Acquisition, Y.L. and S.G.X.

Funding: This research was funded by the National Natural Science Foundation of China (Grant Numbers 21676115, 51609100, 61705020, 61675090 and 61575080), Program for the development of Science and Technology of Jilin province (Grant Numbers 20160101287JC and 20150519024JH), Guangdong Province Science and Technology Projects (Grant Numbers 2015A030310342 and 2015A010103004), and Technology of Education Department of Jilin Province (Grant Number JJKH20170374KJ).

Conflicts of Interest: The authors declare no conflict of interest.

References

1. Zhang, X.F.; Zhu, X.Y.; Feng, J.J.; Wang, A.J. Solvothermal synthesis of N-doped graphene supported PtCo nanodendrites with highly catalytic activity for 4-nitrophenol reduction. *Appl. Surf. Sci.* **2018**, *428*, 798–808. [CrossRef]
2. Bordbar, M.; Negahdar, N.; Nasrollahzadeh, M. Melissa Officinalis L. leaf extract assisted green synthesis of CuO/ZnO nanocomposite for the reduction of 4-nitrophenol and Rhodamine B. *Sep. Purif. Technol.* **2018**, *191*, s295–s300. [CrossRef]
3. Nag, S.; Pramanik, A.; Chattopadhyay, D.; Bhattacharyya, M. Green-fabrication of gold nanomaterials using *Staphylococcus warneri* from Sundarbans estuary: An effective recyclable nanocatalyst for degrading nitro aromatic pollutants. *Environ. Sci. Pollut. Res.* **2017**, *24*, 1–19. [CrossRef] [PubMed]
4. Meziane, D.; Benadda-Kordjani, A.; Nezzal, G.; Benammar, S.; Djadoun, A. Para-nitrophenol reduction on solvothermally prepared cobalt@silica core-shell catalysts. *React. Kinet. Mech. Catal.* **2017**, *122*, 1145–1158. [CrossRef]
5. He, L.L.; Tong, Z.F.; Wang, Z.H.; Chen, M.; Huang, N.; Zhang, W. Effects of calcination temperature and heating rate on the photocatalytic properties of ZnO prepared by pyrolysis. *J. Colloid Interface Sci.* **2017**, *509*, 448–456. [CrossRef] [PubMed]

6. Liu, L.; Yang, W.; Sun, W.; Li, Q.; Shang, J.K. Creation of Cu₂O@TiO₂ composite photocatalysts with p-n heterojunctions formed on exposed Cu₂O facets, their energy band alignment study, and their enhanced photocatalytic activity under visible light illumination. *ACS Appl. Mater. Interfaces* **2015**, *7*, 1465–1476. [[CrossRef](#)] [[PubMed](#)]
7. Andreou, D.; Iordanidou, D.; Tamiolakis, I.; Armatas, G.S.; Lykakis, I.N. Reduction of nitroarenes into aryl amines and *n*-aryl hydroxylamines via activation of NaBH₄ and ammonia-borane complexes by Ag/TiO₂ catalyst. *Nanomaterials* **2016**, *6*, 54. [[CrossRef](#)] [[PubMed](#)]
8. Zhao, X.; Wang, Y.; Feng, W.H.; Lei, H.T.; Li, J. Preparation of Cu(II) porphyrin-TiO₂ composite in one-pot method and research on photocatalytic property. *RSC Adv.* **2017**, *7*, 52738–52746. [[CrossRef](#)]
9. Liu, Y.; Zhang, Y.Y.; Kou, Q.W.; Chen, Y.; Han, D.L.; Wang, D.D.; Lu, Z.Y.; Chen, L.; Yang, J.H.; Xing, S. Eco-friendly seeded Fe₃O₄-Ag nanocrystals: A new type of highly efficient and low cost catalyst for methylene blue reduction. *RSC Adv.* **2018**, *8*, 2209–2218. [[CrossRef](#)]
10. Shah, M.T.; Balouch, A.; Sirajuddin; Pathan, A.A.; Abdullah; Mahar, A.M.; Sabir, S.; Khattak, R.; Umar, A.A. SiO₂ capped Fe₃O₄ nanostructures as an active heterogeneous catalyst for 4-nitrophenol reduction. *Microsyst. Technol.* **2017**, *23*, 5745–5758. [[CrossRef](#)]
11. Svedendahl, M.; Verre, R.; Kall, M. Refractometric Biosensing Based on Optical Phase Flips in Sparse and Short-Range-Ordered Nanoplasmonic Layers. *Light Sci. Appl.* **2014**, *3*, e220. [[CrossRef](#)]
12. Zhu, Z.; Bai, B.; You, O.; Li, Q.; Fan, S. Fano resonance boosted cascaded optical field enhancement in a plasmonic nanoparticle-in-cavity nanoantenna array and its SERS application. *Light Sci. Appl.* **2015**, *4*, e296. [[CrossRef](#)]
13. Wang, P.; Wang, Y.; Tong, L. Graphene-doped polymer nanofibers for low-threshold nonlinear optical waveguiding. *Light Sci. Appl.* **2013**, *2*, e102. [[CrossRef](#)]
14. Li, X.; Xing, L.; Zheng, K.; Wei, P.; Du, L.; Shen, M.; Shi, X. Formation of gold nanostar-coated hollow mesoporous silica for tumor multimodality imaging and photothermal therapy. *ACS Appl. Mater. Interfaces* **2017**, *9*, 5817–5827. [[CrossRef](#)] [[PubMed](#)]
15. Aslam, U.; Chavez, S.; Linic, S. Controlling energy flow in multimetallic nanostructures for plasmonic catalysis. *Nat Nano* **2017**, *12*, 1000–1005. [[CrossRef](#)] [[PubMed](#)]
16. Zhang, Q.; Wang, H. Facet-Dependent Catalytic Activities of Au Nanoparticles Enclosed by High-Index Facets. *ACS Catal.* **2014**, *4*, 4027–4033. [[CrossRef](#)]
17. Karabchevsky, A.; Mosayyebi, A.; Kavokin, A.V. Tuning the chemiluminescence of a luminol flow using plasmonic nanoparticles. *Light Sci. Appl.* **2016**, *5*, 1–7. [[CrossRef](#)]
18. Linnenbank, H.; Grynko, Y.; Forstner, J.; Linden, S. Second harmonic generation spectroscopy on hybrid plasmonic/dielectric nanoantennas. *Light Sci. Appl.* **2016**, *5*, e16013. [[CrossRef](#)]
19. Blum, O.; Shaked, N.T. Prediction of photothermal phase signatures from arbitrary plasmonic nanoparticles and experimental verification. *Light Sci. Appl.* **2015**, *4*, e322. [[CrossRef](#)]
20. Gangarapu, M.; Sarangapany, S.; Veerabali, K.K.; Devipriya, S.P.; Arava, V.B.R. A high-performance catalytic and recyclability of phyto-synthesized silver nanoparticles embedded in natural polymer. *J. Clust. Sci.* **2017**, *28*, 3127–3138. [[CrossRef](#)]
21. Jin, C.J.; Qu, Y.; Wang, M.G.; Han, J.; Hu, Y.M.; Guo, R. Aqueous solution-based Fe₃O₄ seed-mediated route to hydrophilic Fe₃O₄-Au janus nanoparticles. *Langmuir* **2016**, *32*, 4595–4601. [[CrossRef](#)] [[PubMed](#)]
22. Navalón, S.; García, H. Nanoparticles for Catalysis. *Nanomaterials* **2016**, *6*, 123. [[CrossRef](#)] [[PubMed](#)]
23. Maham, M.; Nasrollahzadeh, M.; Sajadi, S.M.; Nekoei, M. Biosynthesis of Ag/reduced graphene oxide/Fe₃O₄ using Lotus Garcinii leaf extract and its application as a recyclable nanocatalyst for the reduction of 4-nitrophenol and organic dyes. *J. Colloid Interface Sci.* **2017**, *497*, 33–42. [[CrossRef](#)] [[PubMed](#)]
24. Jia, L.; Zhou, T.; Xu, J.; Li, F.H.; Xu, Z.Q.; Zhang, B.B.; Guo, S.L.; Shen, X.K.; Zhang, W.S. AuPd bimetallic nanocrystals embedded in magnetic halloysite nanotubes: Facile synthesis and catalytic reduction of nitroaromatic compounds. *Nanomaterials* **2017**, *7*, 333. [[CrossRef](#)] [[PubMed](#)]
25. Xiao, Z.Y.; Zhai, S.R.; Ma, X.P.; Zhao, Z.Y.; Wang, X.; Bai, H.; An, Q.D. Monolithic Cu/C hybrid beads with well developed porosity for reduction of 4-nitrophenol to 4-aminophenol. *New J. Chem.* **2017**, *41*, 13230–13234. [[CrossRef](#)]
26. Zhang, K.H.; Wang, C.W.; Rong, Z.; Xiao, R.; Zhou, Z.; Wang, S.Q. Silver coated magnetic microflowers as an efficient and recyclable Catalyst for catalytic reduction. *New J. Chem.* **2017**, *41*, 14199–141208. [[CrossRef](#)]

27. Sun, J.; Chen, L. Superparamagnetic POT/Fe₃O₄ nanoparticle composites with supported Au nanoparticles as recyclable high-performance nanocatalysts. *Mater. Today Chem.* **2017**, *5*, 43–51. [[CrossRef](#)]
28. Wang, D.M.; Duan, H.C.; Lü, J.H.; Lü, C.L. Fabrication of thermo-responsive polymer functionalized reduced graphene oxide@Fe₃O₄@Au magnetic nanocomposites for enhanced catalytic applications. *J. Mater. Chem. A* **2017**, *5*, 5088–5097. [[CrossRef](#)]
29. Rath, P.C.; Saikia, D.; Mishra, M.; Kao, H.M. Exceptional catalytic performance of ultrafine Cu₂O nanoparticles confined in cubic mesoporous carbon for 4-nitrophenol reduction. *Appl. Surf. Sci.* **2018**, *427*, 1217–1226. [[CrossRef](#)]
30. Meng, G.H.; Zhang, X.Y.; Liu, C.; Wu, J.N.; Guo, X.H.; Liu, Z.Y. Ag quantum dot/montmorillonite composites with fluorescent properties: An efficient catalyst. *Res. Chem. Intermed.* **2017**, *43*, 7137–7145. [[CrossRef](#)]
31. Govan, J.; Gun'ko, Y.K. Recent advances in the application of magnetic nanoparticles as a support for homogeneous catalysts. *Nanomaterials* **2014**, *4*, 222–241. [[CrossRef](#)] [[PubMed](#)]
32. Liu, Y.; Zhang, Y.Y.; Kou, Q.W.; Chen, Y.; Sun, Y.T.; Han, D.L.; Wang, D.D.; Lu, Z.Y.; Chen, L.; Yang, J.H.; Xing, S.G.Z. Highly Efficient, Low-Cost, and Magnetically Recoverable FePt–Ag Nanocatalysts Towards Green Reduction of Organic Dyes. *Nanomaterials* **2018**, *8*, 329. [[CrossRef](#)] [[PubMed](#)]
33. Wysocka, I.; Kowalska, E.; Trzeciński, K.; Lapiński, M.; Nowaczyk, G.; Zielińska-Jurek, A. UV-Vis-Induced Degradation of Phenol over Magnetic Photocatalysts Modified with Pt, Pd, Cu and Au Nanoparticles. *Nanomaterials* **2018**, *2*, 28. [[CrossRef](#)] [[PubMed](#)]
34. Pardo, I.R.; Pons, M.R.; Heredia, A.A.; Usagre, J.V.; Ribera, A.; Galian, R.E.; Prieto, J.P. Fe₃O₄@Au@mSiO₂ as enhancing nanopatform for rose bengal photodynamic activity. *Nanoscale* **2017**, *9*, 10388–10396. [[CrossRef](#)] [[PubMed](#)]
35. Wang, Y.S.; Wang, Y.; Xia, H.; Wang, G.; Zhang, Z.Y.; Han, D.D.; Lv, C.; Feng, J.; Sun, H.B. Preparation of Fe₃O₄-Au-GO nanocomposite for simultaneous treatment of oil/water separation and dye decomposition. *Nanoscale* **2016**, *8*, 17451–17457. [[CrossRef](#)] [[PubMed](#)]
36. Guo, R.; Jiao, T.F.; Xing, R.R.; Chen, Y.; Guo, W.C.; Zhou, J.X.; Zhang, L.X.; Peng, Q.M. Hierarchical AuNPs-Loaded Fe₃O₄/Polymers Nanocomposites Constructed by Electrospinning with Enhanced and magnetically recyclable catalytic capacities. *Nanomaterials* **2017**, *7*, 317. [[CrossRef](#)] [[PubMed](#)]
37. Tedsree, K.; Temnuch, N.; Sriplai, N.; Pinitsoontorn, S. Ag modified Fe₃O₄@TiO₂ magnetic core-shell nanocomposites for photocatalytic degradation of methylene blue. *Mater. Today* **2017**, *4*, 6576–6584. [[CrossRef](#)]
38. Yang, J.H.; Kou, Q.W.; Liu, Y.; Wang, D.D.; Lu, Z.Y.; Chen, L.; Zhang, Y.Y.; Wang, Y.X.; Zhang, Y.J.; Han, D.L.; et al. Effects of amount of benzyl ether and reaction time on the shape and magnetic properties of Fe₃O₄ nanocrystals. *Powder Technol.* **2017**, *319*, 53–59. [[CrossRef](#)]
39. Duan, L.F.; Jia, S.S.; Wang, T.H.; Xue, B.; Wang, Y.Q.; Zhao, L.J. Synthesis and Characterization of hollow Fe₃O₄ submicrospheres by a Simple Solvothermal Synthesis. *Met. Mater. Int.* **2011**, *17*, 801–804. [[CrossRef](#)]
40. Hu, Y.; Yang, J.; Wei, P.; Li, J.C.; Ding, L.; Zhang, G.X.; Shi, X.Y.; Shen, M.W. Facile synthesis of hyaluronic acid-modified Fe₃O₄/Au composite nanoparticles for targeted dual mode MR/CT imaging of tumors. *J. Mater. Chem. B* **2015**, *3*, 9098–9108. [[CrossRef](#)]
41. Wang, C.W.; Li, P.; Wang, J.F.; Rong, Z.; Pang, Y.F.; Xu, J.W.; Dong, P.T.; Xiao, R.; Wang, S.Q. Polyethylenimine-interlayered core-shell-satellite 3D magnetic microspheres as versatile SERS substrate. *Nanoscale* **2015**, *7*, 18694–18707. [[CrossRef](#)] [[PubMed](#)]
42. Yan, F.; Sun, R.Y. Facile Synthesis of Bifunctional Fe₃O₄/Au Nanocomposite and Their Application in Catalytic Reduction of 4-Nitrophenol. *Mater. Res. Bull.* **2014**, *57*, 293–299. [[CrossRef](#)]
43. Liu, Y.; Kou, Q.W.; Wang, D.D.; Chen, L.; Sun, Y.T.; Lu, Z.Y.; Zhang, Y.Y.; Wang, Y.X.; Yang, J.H.; Xing, S. Rational synthesis and tailored optical and magnetic Characteristics of Fe₃O₄-Au composite nanoparticles. *J. Mater. Sci.* **2017**, *52*, 10163–10174. [[CrossRef](#)]
44. Xing, G.Z.; Wang, Y.; Wong, J.I.; Shi, Y.M.; Huang, Z.X.; Li, S.; Yang, H.Y. Hybrid CuO/SnO₂ nanocomposites: Towards cost-effective and high performance binder free lithium ion batteries anode materials. *Appl. Phys. Lett.* **2014**, *105*, 143905. [[CrossRef](#)]
45. Xing, G.Z.; Wang, D.D.; Cheng, C.J.; He, M.; Li, S.; Wu, T. Emergent ferromagnetism in ZnO/Al₂O₃ core-shell nanowires: Towards oxide spinterfaces. *Appl. Phys. Lett.* **2013**, *103*, 022402. [[CrossRef](#)]

46. Sun, Y.; Li, Q. Research of zinc oxide quantum dot light-emitting diodes based on preparation of chemical solutions. *Chin. J. Liq. Cryst. Disp.* **2016**, *31*, 635–642. [[CrossRef](#)]
47. Chen, X.Y.; Tian, Z. Recent progress in terahertz dynamic modulation based on graphene. *Chin. Opt.* **2017**, *10*, 86–97. [[CrossRef](#)]
48. Li, T.; Zhang, M.-L.; Wang, F.; Zhang, D.-M.; Wang, G.-P. Fabrication of optical waveguide amplifiers based on bonding-type NaYF₄: Er nanoparticles-polymer. *Chin. Opt.* **2017**, *10*, 219–225. [[CrossRef](#)]
49. Yang, J.H.; Pan, M.Q.; Shi, R.X.; Yang, L.L.; Wang, J.; Kong, X.W.; Yang, W.Q.; Wang, D.D.; Zhou, Z. Novel Fe₃O₄ hollow microspheres: Nontemplate hydrothermal synthesis, superparamagnetism and biocompatibility. *Nanosci. Nanotech. Lett.* **2017**, *9*, 109–117. [[CrossRef](#)]
50. Shah, S.T.; Yehye, W.A.; Saad, O.; Simarani, K.; Chowdhury, Z.Z.; Alhadi, A.A.; Al-Ani, L.A. Surface functionalization of iron oxide nanoparticles with gallic acid as potential antioxidant and antimicrobial agents. *Nanomaterials* **2017**, *7*, 306. [[CrossRef](#)] [[PubMed](#)]
51. Jin, C.J.; Han, J.; Chu, F.Y.; Wang, X.X.; Guo, R. Fe₃O₄@PANI hybrid shell as multifunctional support for Au nanocatalysts with remarkably improved catalytic performance. *Langmuir* **2017**, *33*, 4520–4527. [[CrossRef](#)] [[PubMed](#)]
52. Miao, P.; Tang, Y.G.; Wang, L. DNA modified Fe₃O₄@Au magnetic nanoparticles as selective probes for simultaneous detection of heavy metal ions. *ACS Appl. Mater. Interfaces* **2017**, *9*, 3940–3947. [[CrossRef](#)] [[PubMed](#)]
53. Baskakov, A.O.; Solov'eva, A.Y.; Ioni, Y.V.; Starchikov, S.S.; Lyubutin, I.S.; Khodos, I.I.; Avilov, A.S.; Gubin, S.P. Magnetic and interface properties of the core-shell Fe₃O₄/Au nanocomposites. *Appl. Surf. Sci.* **2017**, *422*, 638–644. [[CrossRef](#)]
54. Li, X.A.; He, Y.Y.; Sui, H.; He, L. One-step fabrication of dual responsive lignin coated Fe₃O₄ nanoparticles for efficient removal of cationic and anionic dyes. *Nanomaterials* **2018**, *8*, 162. [[CrossRef](#)] [[PubMed](#)]
55. Wang, W.T.; Tang, B.T.; Wu, S.L.; Gao, Z.M.; Ju, B.Z.; Teng, X.X.; Zhang, S.F. Controllable 5-sulfosalicylic acid assisted solvothermal synthesis of monodispersed superparamagnetic Fe₃O₄ nanoclusters with tunable size. *J. Magn. Magn. Mater.* **2017**, *423*, 111–117. [[CrossRef](#)]
56. Ghosh, R.; Pradhan, L.; Devi, Y.P.; Meena, S.S.; Tewari, R.; Kumar, A.; Sharma, S.; Gajbhiye, N.S.; Vatsa, R.K.; Pandey, B.N.; et al. Induction heating studies of Fe₃O₄ magnetic nanoparticles capped with oleic acid and polyethylene glycol for hyperthermia. *J. Mater. Chem.* **2011**, *21*, 13388–13398. [[CrossRef](#)]
57. Ayyappan, S.; Thoguluva, R.R.; John, P. Superior thermal stability of polymer capped Fe₃O₄ magnetic nanoclusters. *J. Am. Ceram. Soc.* **2018**, *101*, 483–491. [[CrossRef](#)]
58. Kazeminezhad, I.; Mosivand, S. Phase Transition of Electrooxidized Fe₃O₄ to γ and α -Fe₂O₃ Nanoparticles Using Sintering Treatment. *Acta Phys. Pol. A* **2014**, *125*, 1210–1214. [[CrossRef](#)]
59. Zhang, M.; Xia, P.; Wang, L.; Zheng, J.; Wang, Y.; Xu, J.; Wang, L. Synthesis and fabrication of CNTs/Fe₃O₄@Pdop@Au nanocables by a facile approach. *RSC Adv.* **2014**, *4*, 44423–44426. [[CrossRef](#)]
60. Mاتيoli, E.; Brinkley, S.; Kelchner, K.M.; Hu, Y.L.; Nakamura, S.; DenBaars, S.; Speck, J.; Weisbuch, C. High-brightness polarized light-emitting diodes. *Light Sci. Appl.* **2012**, *1*, 479–482. [[CrossRef](#)]
61. Li, L.; Guo, W.; Yan, Y.; Lee, S.; Wang, T. Label-free super-resolution imaging of adenoviruses by submerged microsphere optical nanoscopy. *Light Sci. Appl.* **2013**, *2*, e104. [[CrossRef](#)]
62. Wang, D.D.; Wang, W.L.; Huang, M.Y.; Lek, A.; Lam, J.; Mai, Z.H. Failure mechanism analysis and process improvement on time-dependent dielectric breakdown of Cu/ultra-low-k dielectric based on complementary Raman and FTIR spectroscopy study. *AIP Adv.* **2014**, *4*, 107–110. [[CrossRef](#)]
63. Xing, G.; Wang, D.; Yi, J.; Yang, L.; Gao, M.; He, M.; Yang, J.; Ding, J.; Sum, T.C.; Wu, T. Correlated d0 ferromagnetism and photoluminescence in undoped ZnO nanowires. *Appl. Phys. Lett.* **2010**, *96*, 112511. [[CrossRef](#)]
64. Cheng, X.; Zhang, J.; Ding, T.; Wei, Z.; Li, H.; Wang, Z. The effect of an electric field on the thermomechanical damage of nodular defects in dielectric multilayer coatings irradiated by nanosecond laser pulses. *Light Sci. Appl.* **2013**, *2*, e80. [[CrossRef](#)]
65. Wang, D.D.; Xing, G.Z.; Yan, F.; Yan, Y.S.; Li, S. Ferromagnetic (Mn, N)-codoped ZnO nanopillars array: Experimental and computational insights. *Appl. Phys. Lett.* **2014**, *104*, 022412. [[CrossRef](#)]
66. Pincella, F.; Isozaki, K.; Miki, K. A visible light-driven plasmonic photocatalyst. *Light Sci. Appl.* **2014**, *3*, 110–118. [[CrossRef](#)]

67. Xing, G.Z.; Fang, X.S.; Zhang, Z.; Wang, D.D.; Huang, X.; Guo, J.; Liao, L.; Zheng, Z.; Xu, H.R.; Yu, T. Ultrathin single-crystal ZnO nanobelts: Ag-catalyzed growth and field emission property. *Nanotechnology* **2010**, *21*, 255701. [[CrossRef](#)] [[PubMed](#)]
68. Wang, B.; Qu, S. Absorption spectra and near-electric field enhancement effects of Au- and Ag-Fe₃O₄ dimers. *Appl. Surf. Sci.* **2014**, *292*, 1002–1008. [[CrossRef](#)]
69. Zhang, X.; Song, L.; Cai, L.; Tian, X.; Zhang, Q.; Qi, X.; Zhou, W.; Zhang, N.; Yang, F.; Fan, Q.; et al. Optical visualization and polarized light absorption of the single-wall carbon nanotube to verify intrinsic thermal applications. *Light Sci. Appl.* **2015**, *4*, e318. [[CrossRef](#)]
70. Xing, G.Z.; Yi, J.B.; Wang, D.D.; Liao, L.; Yu, T.; Shen, Z.X.; Huan, C.H.A.; Sum, T.C.; Ding, J.; Wu, T. Strong correlation between ferromagnetism and oxygen deficiency in Cr-doped In₂O_{3-δ} nanostructures. *Phys. Rev. B* **2009**, *79*, 174406. [[CrossRef](#)]
71. Xing, G.Z.; Yi, J.B.; Tao, J.G.; Liu, T.; Wong, L.M.; Zhang, Z.; Li, G.P.; Wang, S.J.; Ding, J.; Sum, T.C.; et al. Comparative study of room-temperature ferromagnetism in Cu-doped ZnO nanowires enhanced by structural inhomogeneity. *Adv. Mater.* **2008**, *20*, 3521–3527. [[CrossRef](#)]
72. Tran, V.T.; Zhou, H.J.; Lee, S.; Hong, S.C.; Kim, J.; Jeong, S.; Lee, J. Magnetic-assembly mechanism of superparamagnetoplasmonic nanoparticles on a charged surface. *ACS Appl. Mater. Interfaces* **2015**, *7*, 8650–8658. [[CrossRef](#)] [[PubMed](#)]
73. Ye, M.; Wei, Z.; Hu, F.; Wang, J.X.; Ge, G.L.; Hu, Z.Y.; Shao, M.W.; Lee, S.; Liu, J. Fast assembling microarrays of superparamagnetic Fe₃O₄@Au nanoparticle clusters as reproducible substrates for surface-enhanced Raman scattering. *Nanoscale* **2015**, *7*, 13427–13437. [[CrossRef](#)] [[PubMed](#)]
74. Du, J.J.; Xu, J.W.; Sun, Z.L.; Jing, C.Y. Au nanoparticles grafted on Fe₃O₄ as effective SERS substrates for label-free detection of the 16 EPA priority polycyclic aromatic hydrocarbons. *Anal. Chim. Acta* **2016**, *915*, 81–89. [[CrossRef](#)] [[PubMed](#)]
75. Chen, J.; Pang, S.; He, L.; Nugen, S.R. Highly sensitive and selective detection of nitrite ions using Fe₃O₄@SiO₂/Au magnetic nanoparticles by surface-enhanced Raman spectroscopy. *Biosens. Bioelectron.* **2016**, *85*, 726–733. [[CrossRef](#)] [[PubMed](#)]
76. Li, F.; Yu, Z.F.; Zhao, L.Y.; Xue, T. Synthesis and application of homogeneous Fe₃O₄ core/Au shell nanoparticles with strong SERS effect. *RSC Adv.* **2016**, *6*, 10352–10357. [[CrossRef](#)]
77. Jiang, G.M.; Huang, Y.X.; Zhang, S.; Zhu, H.Y.; Wu, Z.B.; Sun, S.H. Controlled synthesis of Au-Fe heterodimer nanoparticles and their conversion into Au Fe₃O₄ heterostructured nanoparticles. *Nanoscale* **2016**, *8*, 17947–17952. [[CrossRef](#)] [[PubMed](#)]
78. Freitas, M.C.C.; Couto, M.M.; Barroso, M.F.; Pereira, C.; Delos-Santos-Álvarez, N.; Miranda-Ordieres, A.J.; Lobo-Castañón, M.J.; Delerue-Matos, C. Highly monodisperse Fe₃O₄@Au superparamagnetic nanoparticles as reproducible platform for genosensing genetically modified organisms. *ACS Sens.* **2016**, *1*, 1044–1053. [[CrossRef](#)]
79. Abdullaalmamun, M.; Kusumoto, Y.; Zannat, T.; Horieand, Y.; Manaka, H. Au-ultrathin functionalized core-shell (Fe₃O₄@Au) monodispersed nanocubes for a combination of magnetic/plasmonic photothermal cancer cell killing. *RSC Adv.* **2013**, *3*, 7816–7827. [[CrossRef](#)]
80. Zhao, H.Y.; Liu, S.; He, J.; Pan, C.C.; Li, H.; Zhou, Z.Y.; Ding, Y.; Huo, D.; Hu, Y. Synthesis and application of strawberry-like Fe₃O₄-Au nanoparticles as CT-MR dual-modality contrast agents in accurate detection of the progressive liver disease. *Biomaterials* **2015**, *51*, 194–207. [[CrossRef](#)] [[PubMed](#)]
81. Wang, L.Y.; Luo, J.; Fan, Q.; Suzuki, M.; Suzuki, I.S.; Engelhard, M.H.; Lin, Y.H.; Kim, N.; Wang, J.Q.; Zhong, C.J. Monodispersed Core-Shell Fe₃O₄@Au Nanoparticles. *J. Phys. Chem. B* **2005**, *109*, 21593–21601. [[CrossRef](#)] [[PubMed](#)]
82. Hong, L.R.; Zhao, J.; Lei, Y.M.; Yuan, R.; Zhuo, Y. Efficient electrochemiluminescence from Ru(bpy)₃²⁺ enhanced by three-layer porous Fe₃O₄@SnO₂@Au nanoparticles for label-free and sensitive bioanalysis. *Electrochim. Acta* **2017**, *241*, 291–298. [[CrossRef](#)]
83. Wang, Y.; Li, H.; Zhang, J.J.; Yan, X.Y.; Chen, Z.X. Fe₃O₄ and Au nanoparticles dispersed on graphene support as a highly active catalyst toward the reduction of 4-nitrophenol. *Phys. Chem. Chem. Phys.* **2016**, *18*, 615–623. [[CrossRef](#)] [[PubMed](#)]
84. Xia, Q.D.; Fu, S.S.; Ren, G.J.; Chai, F.; Jiang, J.J.; Qu, F.Y. Fabrication of Fe₃O₄@Au hollow spheres with recyclable and efficient catalytic properties. *New J. Chem.* **2016**, *40*, 818–824. [[CrossRef](#)]

85. Yu, L.; Zhang, Y.T.; Chen, R.; Zhang, D.H.; Wei, X.H.; Chen, F.; Wang, J.X.; Xu, M.T. A highly sensitive resonance light scattering probe for Alzheimer's amyloid- β peptide based on $\text{Fe}_3\text{O}_4/\text{Au}$ composites. *Talanta* **2015**, *131*, 475–479. [[CrossRef](#)] [[PubMed](#)]
86. Hou, Y.H.; Yuan, H.L.; Chen, H.; Shen, J.H.; Li, L.C. Controlled fabrication and microwave absorbing mechanism of hollow $\text{Fe}_3\text{O}_4/\text{C}$ microspheres. *Sci. China Chem.* **2017**, *60*, 740–747. [[CrossRef](#)]
87. Kwizera, E.A.; Chaffin, E.; Wang, Y.M.; Huang, X.H. Synthesis and properties of magnetic-optical core-shell nanoparticles. *RSC Adv.* **2017**, *7*, 17137–17153. [[CrossRef](#)] [[PubMed](#)]
88. Mitra, A.; Mohapatra, J.; Meena, S.S.; Tomy, C.V.; Aslam, M. Verwey Transition in Ultrasmall-sized Octahedral Fe_3O_4 Nanoparticles. *J. Phys. Chem. C* **2012**, *118*, 19356–19362. [[CrossRef](#)]
89. Zhu, Y.M.; Zhou, X.W.; Chen, D.S.; Li, F.; Xue, T.; Farag, A.S. Ternary $\text{Fe}_3\text{O}_4/\text{PANI}/\text{Au}$ nanocomposites as a magnetic catalyst for degradation of organic dyes. *Sci. China Technol. Sci.* **2017**, *60*, 749–757. [[CrossRef](#)]
90. Zhang, X.; Ding, S.N. Sandwich-structured electrogenerated chemiluminescence immunosensor based on dual-stabilizers-capped CdTe quantum dots as signal probes and $\text{Fe}_3\text{O}_4/\text{Au}$ nanocomposites as magnetic separable carriers. *Sensor. Actuators B Chem.* **2017**, *240*, 1123–1133. [[CrossRef](#)]
91. Hu, R.; Zheng, M.X.; Wu, J.C.; Li, C.; Shen, D.Q.; Yang, D.; Li, L.; Ge, M.F.; Chang, Z.M.; Dong, W.F. Core-shell magnetic gold nanoparticles for magnetic field-enhanced radio-photothermal therapy in cervical cancer. *Nanomaterials* **2017**, *7*, 111. [[CrossRef](#)] [[PubMed](#)]
92. Wang, Z.Y.; Su, R.N.; Wang, D.; Wang, J.X.; Pu, Y.; Chen, J.F. Sulfurized graphene as efficient metal-free catalysts for reduction of 4-nitrophenol to 4-aminophenol. *Ind. Eng. Chem. Res.* **2017**, *56*, 13610–13617. [[CrossRef](#)]
93. Liu, X.; Li, Y.; Xing, Z.; Zhao, X.H.; Liu, N.N.; Chen, F.Y. Monolithic carbon foam-supported Au nanoparticles with excellent catalytic performance in a fixed-bed system. *New J. Chem.* **2017**, *41*, 15027–15032. [[CrossRef](#)]



© 2018 by the authors. Licensee MDPI, Basel, Switzerland. This article is an open access article distributed under the terms and conditions of the Creative Commons Attribution (CC BY) license (<http://creativecommons.org/licenses/by/4.0/>).